

AFRL-IF-RS-TR-2005-317
Final Technical Report
September 2005



INTEGRATED TRANSCEIVER CHIP APPLICATION IN FREE SPACE OPTICAL COMMUNICATION

APIC Corporation

APPROVED FOR PUBLIC RELEASE; DISTRIBUTION UNLIMITED.

**AIR FORCE RESEARCH LABORATORY
INFORMATION DIRECTORATE
ROME RESEARCH SITE
ROME, NEW YORK**

STINFO FINAL REPORT

This report has been reviewed by the Air Force Research Laboratory, Information Directorate, Public Affairs Office (IFOIPA) and is releasable to the National Technical Information Service (NTIS). At NTIS it will be releasable to the general public, including foreign nations.

AFRL-IF-RS-TR-2005-317 has been reviewed and is approved for publication

APPROVED: /s/

ROBERT L. KAMINSKI
Project Engineer

FOR THE DIRECTOR: /s/

WARREN H. DEBANY, JR., Technical Advisor
Information Grid Division
Information Directorate

REPORT DOCUMENTATION PAGE			Form Approved OMB No. 074-0188	
Public reporting burden for this collection of information is estimated to average 1 hour per response, including the time for reviewing instructions, searching existing data sources, gathering and maintaining the data needed, and completing and reviewing this collection of information. Send comments regarding this burden estimate or any other aspect of this collection of information, including suggestions for reducing this burden to Washington Headquarters Services, Directorate for Information Operations and Reports, 1215 Jefferson Davis Highway, Suite 1204, Arlington, VA 22202-4302, and to the Office of Management and Budget, Paperwork Reduction Project (0704-0188), Washington, DC 20503				
1. AGENCY USE ONLY (Leave blank)		2. REPORT DATE SEPTEMBER 2005	3. REPORT TYPE AND DATES COVERED Final Apr 04 – Apr 05	
4. TITLE AND SUBTITLE INTEGRATED TRANSCEIVER CHIP APPLICATION IN FREE SPACE OPTICAL COMMUNICATION			5. FUNDING NUMBERS C - FA8750-04-C-0035 PE - 62500F PR - 5082 TA - FS WU - OC	
6. AUTHOR(S) James Chan				
7. PERFORMING ORGANIZATION NAME(S) AND ADDRESS(ES) APIC Corporation 5800 Uplander Way Culver City California 90230-6608			8. PERFORMING ORGANIZATION REPORT NUMBER N/A	
9. SPONSORING / MONITORING AGENCY NAME(S) AND ADDRESS(ES) Air Force Research Laboratory/IFGA 525 Brooks Road Rome New York 13441-4505			10. SPONSORING / MONITORING AGENCY REPORT NUMBER AFRL-IF-RS-TR-2005-317	
11. SUPPLEMENTARY NOTES AFRL Project Engineer: Robert L. Kaminski/IFGA/(315) 330-1867/ Robert.Kaminski@rl.af.mil				
12a. DISTRIBUTION / AVAILABILITY STATEMENT APPROVED FOR PUBLIC RELEASE; DISTRIBUTION UNLIMITED.				12b. DISTRIBUTION CODE
13. ABSTRACT (Maximum 200 Words) The final report describes the design, fabrication, test methods, and performance analysis of a laser array. The developed multi-channel wavelength division multiplexing (WDM) laser array chip provides for hybrid-integration with an Arrayed Waveguide Grating (AWG) based multiplexer (Mux) to form a transceiver chip on silicon-on-insulator (SOI) or silica platform. The developed WDMA laser array chip will be able to support different data interfaces and protocols. In addition, this program further developed Photonics Integrated Circuits (PICs) technology. PICs provide specific military benefits for reliable (less number of interconnects), smaller foot print, and light weight communication subsystems at the theater level, and multiplexing of multiple communication links onto a common free-space laser link between ground uses and airborne vehicles such as Unmanned Air Vehicles.				
14. SUBJECT TERMS Free Space Optical Communications, Laser Array, Integrated Optical Transceiver				15. NUMBER OF PAGES 35
				16. PRICE CODE
17. SECURITY CLASSIFICATION OF REPORT UNCLASSIFIED	18. SECURITY CLASSIFICATION OF THIS PAGE UNCLASSIFIED	19. SECURITY CLASSIFICATION OF ABSTRACT UNCLASSIFIED	20. LIMITATION OF ABSTRACT UL	

TABLE OF CONTENTS

1	INTRODUCTION.....	1
2	LASER ARRAY DESIGN AND SPECIFICATIONS	1
2.1	WAFER EPITAXIAL DESIGN.....	1
2.2	LASER STRUCTURE	6
2.3	LASER ARRAY DESIGN AND SPECIFICATIONS	8
2.4	CHALLENGES AND TECHNICAL APPROACHES	9
3	LASER ARRAY FABRICATIONS	12
3.1	WAFER GROWTH.....	12
3.2	QUANTUM WELL INTERMIXING	13
3.3	GRATING FABRICATIONS.....	16
3.4	DBR LASER FABRICATIONS.....	18
4	TEST METHODS OF LASER ARRAY CHARACTERISTICS	21
4.1	LASER SPECTRUM TESTS	21
4.2	LASER P-I AND I-V TESTS	21
4.3	LASER DATA RATE AND FREQUENCY RESPONSE TESTS.....	22
4.4	LASER LINEWIDTH TESTS	23
5	TESTED RESULTS.....	24
5.1	WAVELENGTH, CHANNEL SPACE, AND SIDE - MODE SUPPRESSION RATIO	24
5.2	THRESHOLD CURRENTS AND OUTPUT POWERS	25
5.3	DATA RATE AND -3 dB BANDWIDTH	26
5.4	LASER LINEWIDTH	27
6	SUMMARY	28

LIST OF FIGURES

FIGURE 1 QUANTUM WELL NUMBER DEPENDENCE OF LASER POWER FOR LASER CAVITY LENGTHS $L=500\text{ }\mu\text{m}$ (CIRCLES), AND $250\text{ }\mu\text{m}$ (SQUARES). (FROM SEMICONDUCTOR SCIENCE TECHNOLOGY, VOL.14, P.1069, 1999 [1].)	2
FIGURE 2 QUANTUM WELL NUMBER DEPENDENCE OF LASER THRESHOLD CURRENT. THE SOLID LINE IS CALCULATED AND THE CIRCLES ARE MEASURED RESULTS AT $20\text{ }^{\circ}\text{C}$ FOR LASERS WITH CAVITY LENGTHS OF 350, 700, AND $1050\text{ }\mu\text{m}$ AND CLEAVED FACETS ($R1=R2=0.28$). (FROM IEEE J. SELECTED TOPICS IN QUANTUM ELECTRONICS, VOL.5, P.420, 1999 [2].)	2
FIGURE 3 STRAIN DEPENDENCE OF T_0 .	3
FIGURE 4 STRAIN DEPENDENCE OF LASER THRESHOLD CURRENT	3
FIGURE 5 CALCULATED GAIN SPECTRUM OF THE WAFERS	5
FIGURE 6 CALCULATED BAND GAP ENERGY DIAGRAM.	5
FIGURE 7 CALCULATED INDEX PROFILE IN THE LASERS.	6
FIGURE 8 SCHEMATIC DIAGRAM OF INDIVIDUAL DBR LASERS.	6
FIGURE 9 CALCULATED LASER MODE SPECTRUM AT BIAS OF 50 MA.	7
FIGURE 10 CALCULATED LASER NEAR FIELD DISTRIBUTIONS IN VERTICAL DIRECTION (PERPENDICULAR TO THE JUNCTION), AND CROSS SECTION.	7
FIGURE 11 SCHEMATIC QUANTUM WELL ENERGY (A) BEFORE QWI, AND (B) AFTER QWI.	9
FIGURE 12 SCHEMATIC DIAGRAM OF THE WAFER WITH DIFFERENT SiO_2 FILM THICKNESSES FOR ION IMPLANTATION, AND CORRESPONDING GAIN SPECTRA FOR EACH AREA.	10
FIGURE 13 SCHEMATIC DIAGRAM OF INTEGRATED LASER ARRAY AND CORRESPONDING LASER SPECTRA.	11
FIGURE 14 SCHEMATIC DIAGRAM OF WAFER LAYER STRUCTURE.	12
FIGURE 15 FLOW CHART OF QUANTUM WELL INTERMIXING	14
FIGURE 16 SCHEMATIC DIAGRAM OF THE SET-UP FOR PL TESTS OF THE WAFERS	15
FIGURE 17 PL SPECTRA OF THE WAFER AFTER QW INTERMIXING. EACH SPECTRUM WAS TAKEN FROM THE AREA WITH DIFFERENT THICKNESSES OF THE SiO_2/SiN FILMS.	16
FIGURE 18 FLOW CHART OF GRATING FABRICATIONS	17
FIGURE 19 SEM PICTURE OF E-BEAM GENERATED GRATING PATTERN	18
FIGURE 20 FLOW CHART OF DBR LASER FABRICATIONS.	20
FIGURE 21 PICTURE OF LASER ARRAY (TOP VIEW).	20
FIGURE 22 SCHEMATIC DIAGRAM OF SET-UP FOR LASER SPECTRUM TESTS.	21
FIGURE 23 SCHEMATIC DIAGRAM OF SET-UP FOR LASER P-I AND I-V TESTS.	22
FIGURE 24 SCHEMATIC DIAGRAM OF SET-UP FOR LASER DATA RATE TESTS.	22
FIGURE 25 SCHEMATIC DIAGRAM OF SET-UP FOR LASER FREQUENCY RESPONSE TESTS.	23
FIGURE 26 SCHEMATIC DIAGRAM OF SET-UP FOR LASER LINEWIDTH TESTS.	24
FIGURE 27 LASER ARRAY SPECTRUM.	25
FIGURE 28 LASER P-I CHARACTERISTICS (A) TESTED P-I FROM 3 DIFFERENT LASERS IN THE LASER ARRAY (B) MAXIMUM OUTPUT POWER TESTED FROM A LASER IN THE LASER ARRAY	25
FIGURE 29 LASER I-V CHARACTERISTICS TESTED FROM A LASER IN THE LASER ARRAY.	26
FIGURE 30 LASER FREQUENCY RESPONSE.	26
FIGURE 31 5 GB/S EYE PATTERN TESTED FROM A LASER IN THE ARRAY.	27
FIGURE 32 LINE SHAPE OF THE HETERODYNE SIGNAL TESTED FROM A LASER IN THE ARRAY.	27

LIST OF TABLES

TABLE 1 - WAFER STRUCTURE	4
TABLE 2 - DESIGNED LASER ARRAY SPECIFICATIONS.....	8
TABLE 3 - LIST OF TESTED LASER ARRAY PERFORMANCE AND DESIGNED SPECIFICATIONS.	28

1 Introduction

APIC has successfully completed the project entitled “Integrated Transceiver Chip Application in Free Space Optical Communication Phase I”. Our test results show that the laser array performance meets the design specifications as called out in the contract. This report presents the laser array design, fabrication, test methods, and analyzes of tested laser performance. Since the design and fabrication of the laser arrays have been detailed in previous monthly and quarterly reports, this document will provide only a brief description for these two parts (i.e. Section 2 and Section 3). The majority of the document will be dedicated to describing the test methods, Section 4 and analyzing the test results, Section 5.

The report is organized as follows:

- Section 2 - laser array design;
- Section 3 - laser array fabrications;
- Section 4 - test methods;
- Section 5 - tested laser array
- Section 6 - summary

2 Laser Array Design and Specifications

2.1 Wafer Epitaxial Design

The wafer structure is very important in determining the laser performance. An ideal laser should have low threshold current density, high quantum efficiency, good temperature characteristics, high power, and small beam divergence. To fabricate such a laser, we designed the optimum wafer structure with 5 quantum wells. The Quantum Well (QW) with 1% compressive strain and two separate, confinement layers was used to achieve a large optical confinement factor.

If a wafer has a small quantum well number, it will be difficult to get high output power from that wafer. The optical confinement factor in the well will increase with the well number; this would be effective for low threshold current. Some authors have studied quantum well number dependence on laser power and threshold as shown in Figures 1 and 2. The results show that a large well number can achieve higher power and larger T_0 . However, as the well number increases a point is reached where saturation occurs, the quantum efficiency decreases, and threshold current increases. The main reason is as quantum well number increases, you also see an increasing material loss and laser beam. Figures 1 and 2 clearly show that 4 or 5 quantum wells will be the optimum choice to get high laser power and low threshold current.

Many theoretical and experimental results have shown that the wafer with strained quantum wells could improve a laser performance; some examples are low threshold current, high efficiency, high modulation frequency, and good temperature characteristics. It has been demonstrated that lasers with compressive strain could get better T_0 than that of the tensile strain, and minimum threshold of tensile strained QWs is achieved over a narrower range of strain than that in the compressive case as shown in Figures 3 and 4. The figures clearly show

that the quantum wells with 1% compressive strain have optimum temperature characteristics and low threshold current.

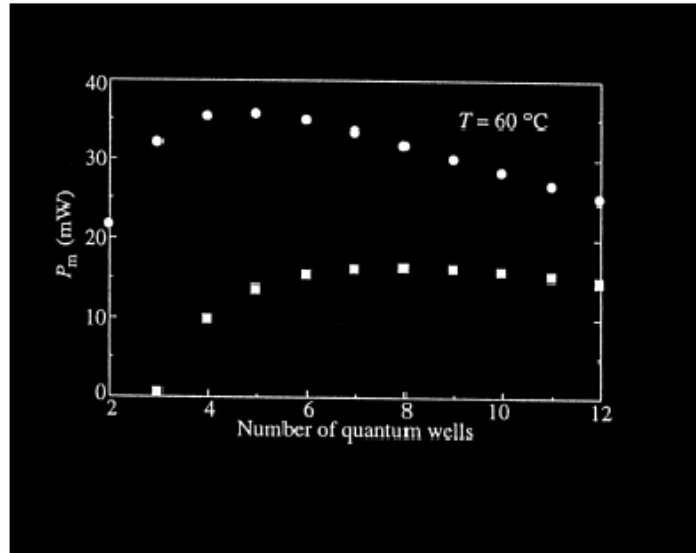


Figure 1
Quantum well number dependence of laser power for laser cavity lengths $L=500 \mu\text{m}$ (circles), and $250 \mu\text{m}$ (squares). (From Semiconductor Science Technology, Vol.14, P.1069, 1999 [1].)

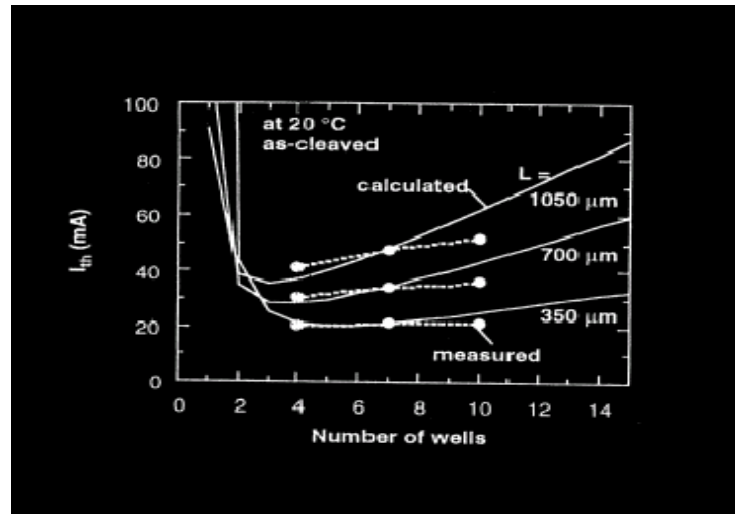


Figure 2
Quantum well number dependence of laser threshold current. The solid line is calculated and the circles are measured results at $20 \text{ }^{\circ}\text{C}$ for lasers with cavity lengths of 350 , 700 , and $1050 \mu\text{m}$ and cleaved facets ($R_1=R_2=0.28$). (From IEEE J. Selected Topics in Quantum Electronics, Vol.5, P.420, 1999 [2].)

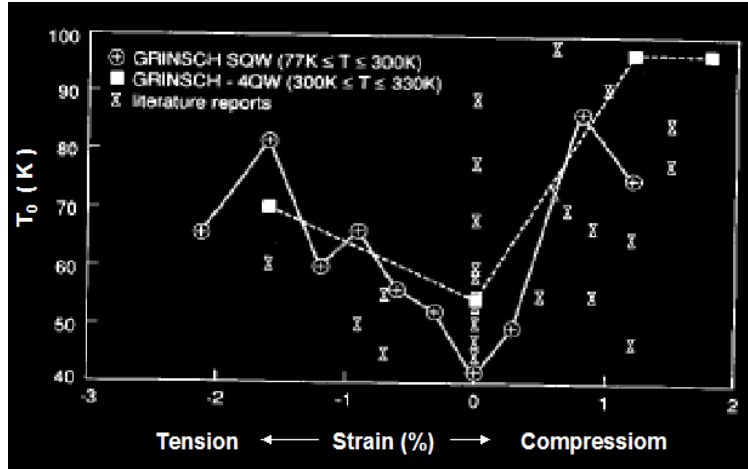


Figure 3
Strain dependence of T_0 .
(From IEEE J. Quantum Electronics, Vol.30, P.477, 1994 [3].).

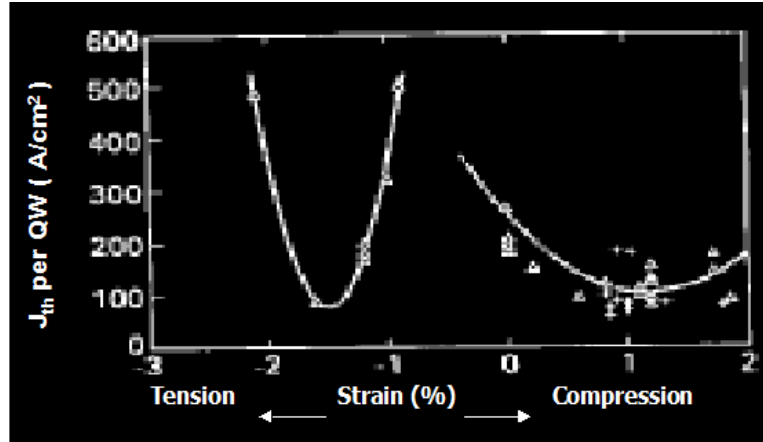


Figure 4
Strain dependence of laser threshold current
(From IEEE J. Quantum Electronics, Vol.30, P.477, 1994 [3].)

The well thickness and barrier height in the quantum wells also play important roles in determining laser performance. Thicker wells are favorable because they provide large electron confinement. However, if the well thickness is too large, the high order levels in the valence band are closer to the fundamental level, which may cause excess carrier at high temperature. Higher barriers could provide good carrier confinement, but it is limited by laser emitting wavelength, refractive index, and optimum strain. For this project APIC used the well thickness of 6 nm, and a barrier height of 0.31 eV.

Table 1 shows the wafer structure. The active region consists of five, 6 nm compressively strained (1%) quantum wells separated by four, 12 nm barriers with tensile strained (0.2%). The thickness of the two outer barriers is 17 nm. The active region is sandwiched between two separate confinement layers with 40 nm Q (1.156 μm), and 100 nm Q (1.05 μm), respectively. The two separate confinement layers could be used to achieve a narrow laser beam with a large optical confinement factor, and the resulting low threshold current. An

etch stop layer composed of 50 nm is for selective etching to fabricate the laser ridge, and the top InGaAs layer with high Zn doped density is for p- contact.

Material	Thickness (nm)	Doped density (1/cm ³)	Comment
P ⁺ - Ga _{0.47} In _{0.53} As	100	Zn: 2E+19	Contact
P - InP	1000	Zn: 7E+17	Upper cladding
P – Ga _{0.2} In _{0.8} As _{0.435} P _{0.565} Lattice matched to InP	50	Zn: 7E+17	Etching stop layer
P - InP	90	Zn: 5E+17	Upper cladding
InP	110	Undoped	Upper cladding
GaInAsP ($\lambda_g=1.05 \mu\text{m}$) lattice matched to InP	100	Undoped	SCL2
GaInAsP ($\lambda_g=1.156 \mu\text{m}$) Lattice matched to InP	40	Undoped	SCL1
Ga _{0.29} In _{0.71} As _{0.55} P _{0.45} 0.2% tensile strain	17	Undoped	First barrier
Ga _{0.27} In _{0.73} As _{0.87} P _{0.13} 1% compressively strain	6	Undoped	Well x 5
Ga _{0.29} In _{0.71} As _{0.55} P _{0.45} 0.2% tensile strain	12	Undoped	
Ga _{0.29} In _{0.71} As _{0.55} P _{0.45} 0.2% tensile strain	17	Undoped	Barrier x 4
Ga _{0.29} In _{0.71} As _{0.55} P _{0.45} 0.2% tensile strain	17	Undoped	Last barrier
GaInAsP ($\lambda_g=1.156 \mu\text{m}$) Lattice matched to InP	40	Undoped	SCL1
GaInAsP ($\lambda_g=1.05 \mu\text{m}$) Lattice matched to InP	100	Undoped	SCL2
N - InP	1200	Si: 1E+18	lower cladding
N ⁺ - InP	500	Si: 4E+18	Buffer
N ⁺ - InP		Si: 4E+18	Substrate

Table 1 - Wafer Structure

We have used commercial software, PICS3D from Crosslight Software Inc., to calculate the gain spectrum of the wafer, which is plotted in Figure 5. The gain peak is at the wavelength of ~1.570 μm in the figure, which will meet the requirement of the longest wavelength in the laser arrays.

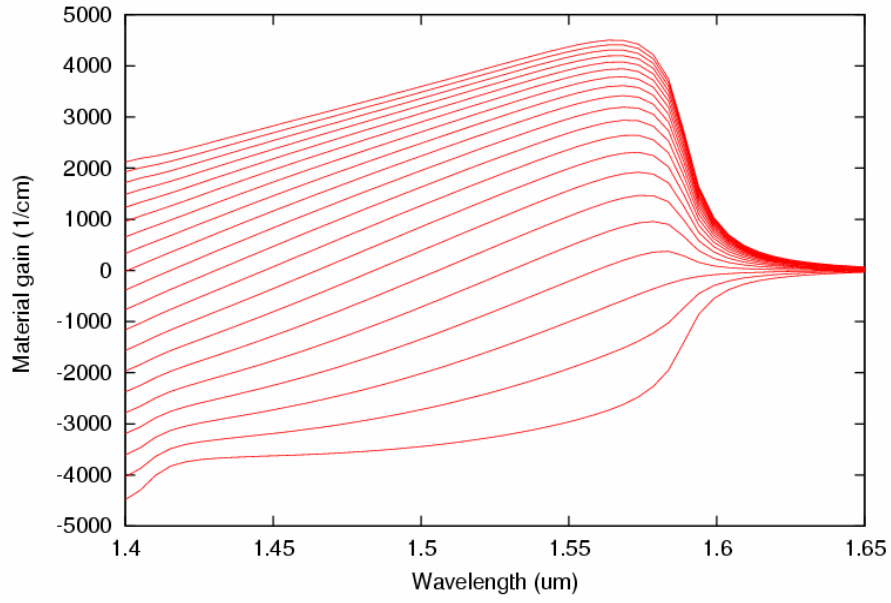


Figure 5
Calculated gain spectrum of the wafers

Figures 6 and 7 are the calculated band gap energy diagram and index profile, respectively. Two separate-confinement layers with different index have been clearly shown in Figure 7.

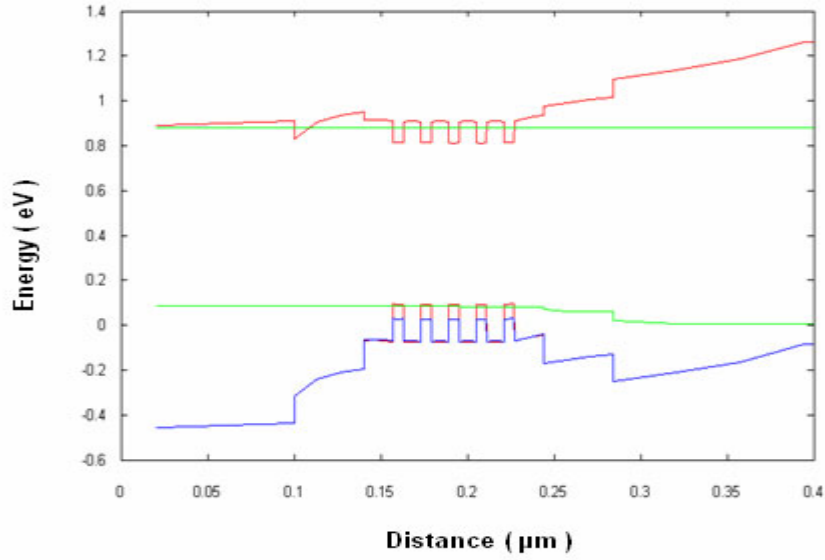


Figure 6
Calculated band gap energy diagram.

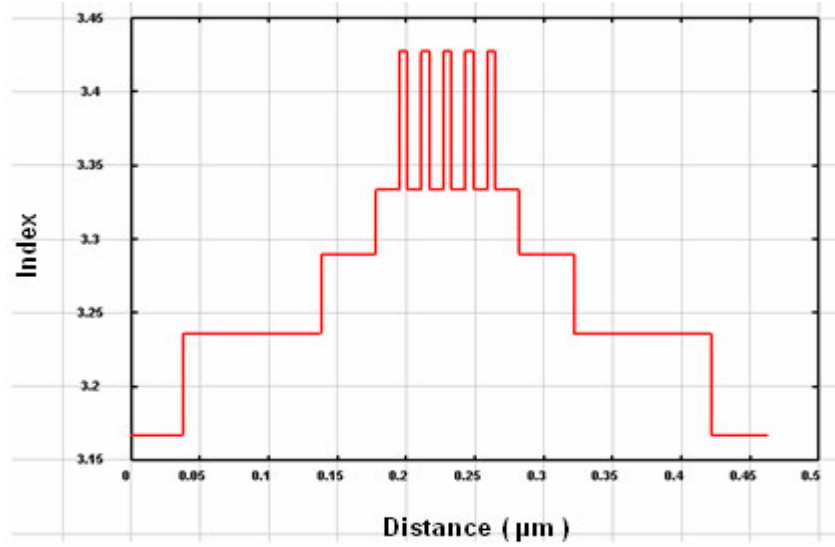


Figure 7
Calculated index profile in the lasers.

2.2 Laser structure

The laser array consists of a group of Distributed-Bragg-Reflector (DBR) lasers. Figure 8 is the schematic diagram of our individual DBR laser with a first-order grating. The DBR is placed at one end of the laser stripe as a backside mirror, and a cleaved facet at the other end is used as the front mirror. The gain region length is 500 μm , and the DBR region length is 250 μm .

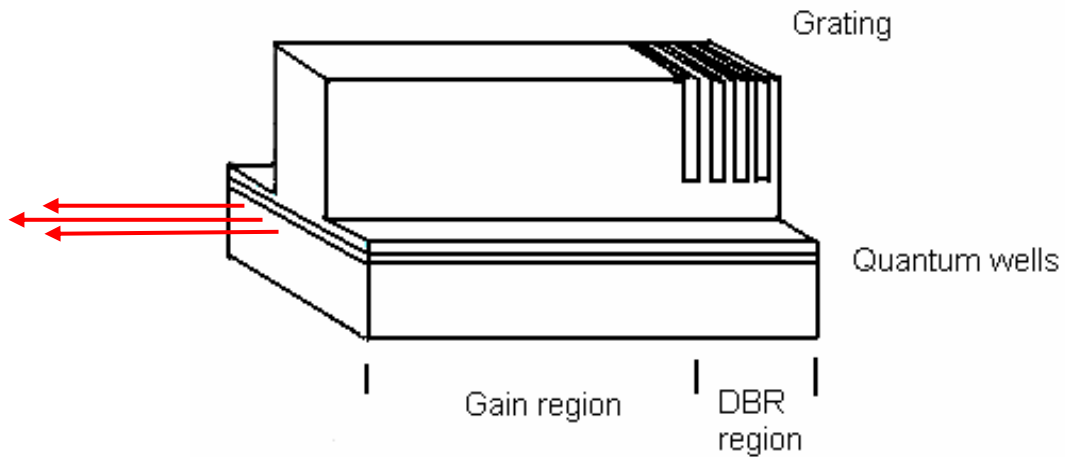


Figure 8
Schematic diagram of individual DBR lasers.

We have also used PICS3D to simulate the laser performance for the above laser structure. Figure 9 is the calculated laser mode spectrum at bias of 50 mA, and a side-mode suppression ratio of 35 dB has been obtained.

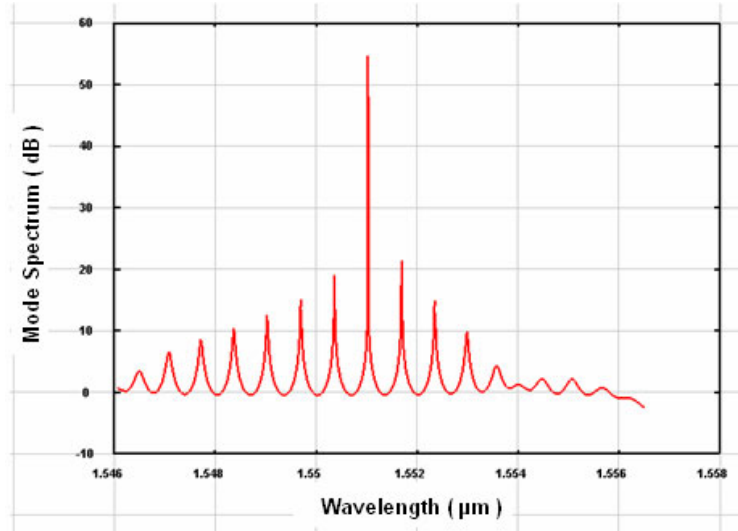


Figure 9
Calculated laser mode spectrum at bias of 50 mA.

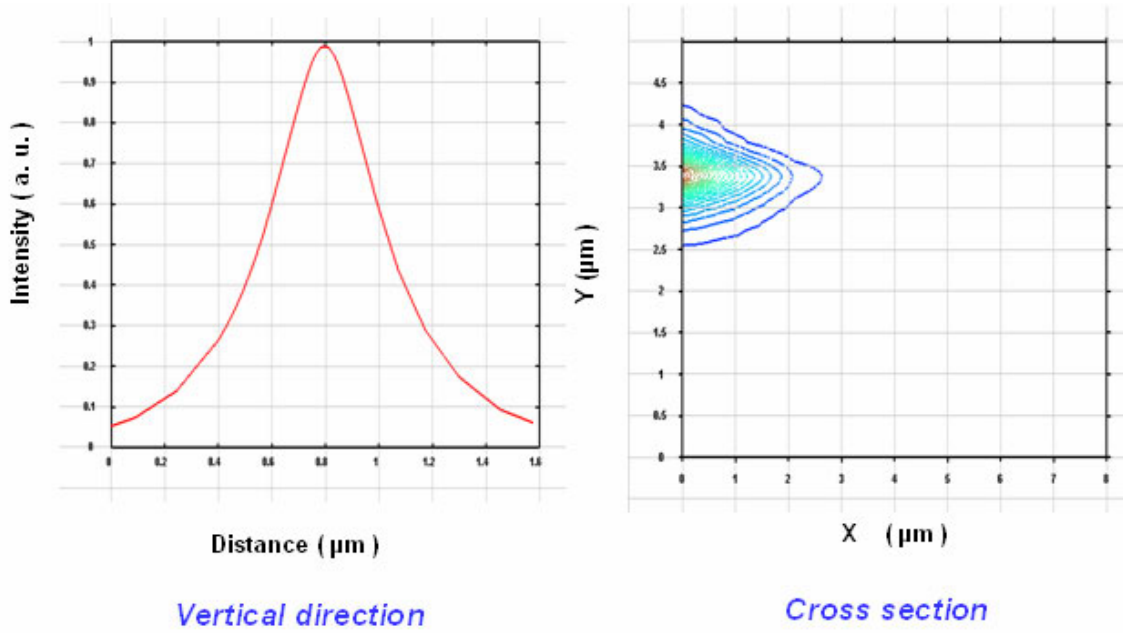


Figure 10
Calculated laser near field distributions in vertical direction
(perpendicular to the junction), and cross section.

The calculated laser near field distributions is plotted in Figure. 10. The figures shown at the left and right side are the laser near filed in vertical direction (perpendicular to the junction), and the cross section, respectively. They show that it is a single mode, and the laser near field is a good Gauss distribution.

2.3 Laser array design and specifications

The lasing wavelength of each laser in an array coincides with the Bragg wavelength λ of the grating given by [4]

$$\lambda = 2 n_{\text{eff}} \Lambda \quad (1)$$

where Λ is the grating pitch and n_{eff} is the effective index of the waveguide. To obtain multiple wavelengths in an array, the grating pitches for individual lasers are varied on the wafer during the grating fabrication.

In the initial proposal for Phase I, the target channel spacing of the laser arrays was 3.2 nm, which corresponds to 400 GHz. However, the best resolution of the e-beam writer that we used is 2.5 nm, and the service charge for a high-resolution e-beam writer was out of the scope of the requested budget. We did not have enough money to fabricate the laser array with channel spacing of 3.2 nm in Phase I. Based on the direction given at the February program review in Honolulu; we designed a laser array with 3 channels. The multi-channel laser arrays with small channel spacing will be designed and fabricated in Phase II.

The minimum grating pitch difference between two neighboring lasers depends on the E-beam writer resolution, and the channel spacing $\Delta\lambda$ of the laser arrays was calculated based on the following relation:

$$\Delta\lambda = 2 n_{\text{eff}} \Delta\Lambda \quad (2)$$

Where $\Delta\Lambda$ is the grating pitch difference between two channels, the value of the effect index is 3.0 to 3.2, and depends on the waveguide structure. If $\Delta\Lambda = 2.5$ nm and $n_{\text{eff}} = 3.0$ to 3.2, from Equation (2), the channel space $\Delta\lambda$ will be 15 to 16 nm. The laser array design specifications are listed in Table 2.

Channel number	3
Channel spacing	15 nm
Output power per channel	≥ 1 mW
Side mode suppression ratio	≥ 30 dB
Threshold current per channel	≤ 30 mA
Laser line width at half intensity	≤ 0.1 Å
Data rate per channel	2.5 Gbps
Distance between two channels	250 μm

Table 2 - Designed laser array specifications

2.4 Challenges and technical approaches

The wavelengths of the laser array cover a region of $\sim 30\text{nm}$. Because the limitation of gain spectrum width and gain change with wavelength, it will be difficult to get equal power and threshold current for different lasers integrated on a single chip.

To solve this challenge, we used Quantum Well Intermixing (QWI) technology to fabricate the wafer with multi – peak – wavelength gain. In this technology, the bandgap of a QW structure is modified selectively after growth. The QWI mechanism is based on the fact that a QW is an inherently metastable system due to the large concentration gradient of atomic species across the well and barrier interface. At high temperature, significant diffusion of atomic species will occur, resulting in an interdiffusion of the well and barrier materials and the modification of the QW shape. Therefore, the QW bandgap energy will be blue shifted as shown in Figure. 11. It has been demonstrated that the intermixing process can be greatly enhanced by the presence of impurities or defects in the vicinity of the interfaces of the QWs, allowing intermixing to occur at temperatures that are substantially lower than what is normally required.

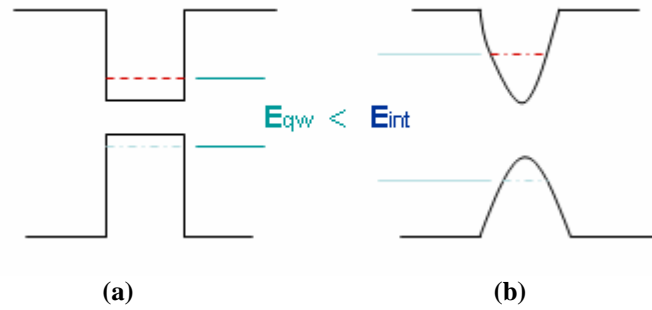


Figure 11
Schematic quantum well energy (a) before QWI, and (b) after QWI.

There are several techniques used to accomplish QWI. They are impurity-induced disordering (IID) [5,6], impurity-free vacancy-enhanced disordering (IFVD) [7], photo-absorption-induced disordering (PAID) [8,9], and implantation-enhanced interdiffusion (IEI) [10-12].

The IID method uses impurities, commonly dopants, to change the equilibrium defect concentration, which is dependent on the Fermi level, to enhance the group-III or group-V self-diffusion in the crystal, thereby promoting the intermixing. Although this technique has been shown to be successful, the introduction of dopants used to promote intermixing could have adverse effects on the electrical nature of the device structure.

The IFVD method uses the postgrowth introduction of vacancies, which during a subsequent thermal process allows the vacancies to diffuse through the lattice where adjacent atoms exchange places, thereby accomplishing the intermixing. This method commonly uses a SiO₂ layer to promote the out diffusion of Ga, creating and diffusing vacancies during the anneal. This can be applied to the INP material system with the use of InGaAs cap on which the SiO₂ layer is deposited. The drawback of this method is that the characteristics of the top InGaAs layer will be changed after QWI.

The PAID technique uses localized heating of the quantum-well structure through laser irradiation to accomplish QWI. Although this technique yields high material quality, the spatial resolution is poor.

The IEI method uses the implantation enhanced interdiffusion method, which relies on the diffusion of point defects created during an ion implantation. This method has been shown to have good spatial resolution, and to be controllable using anneal time, temperature, and ion dose etc.

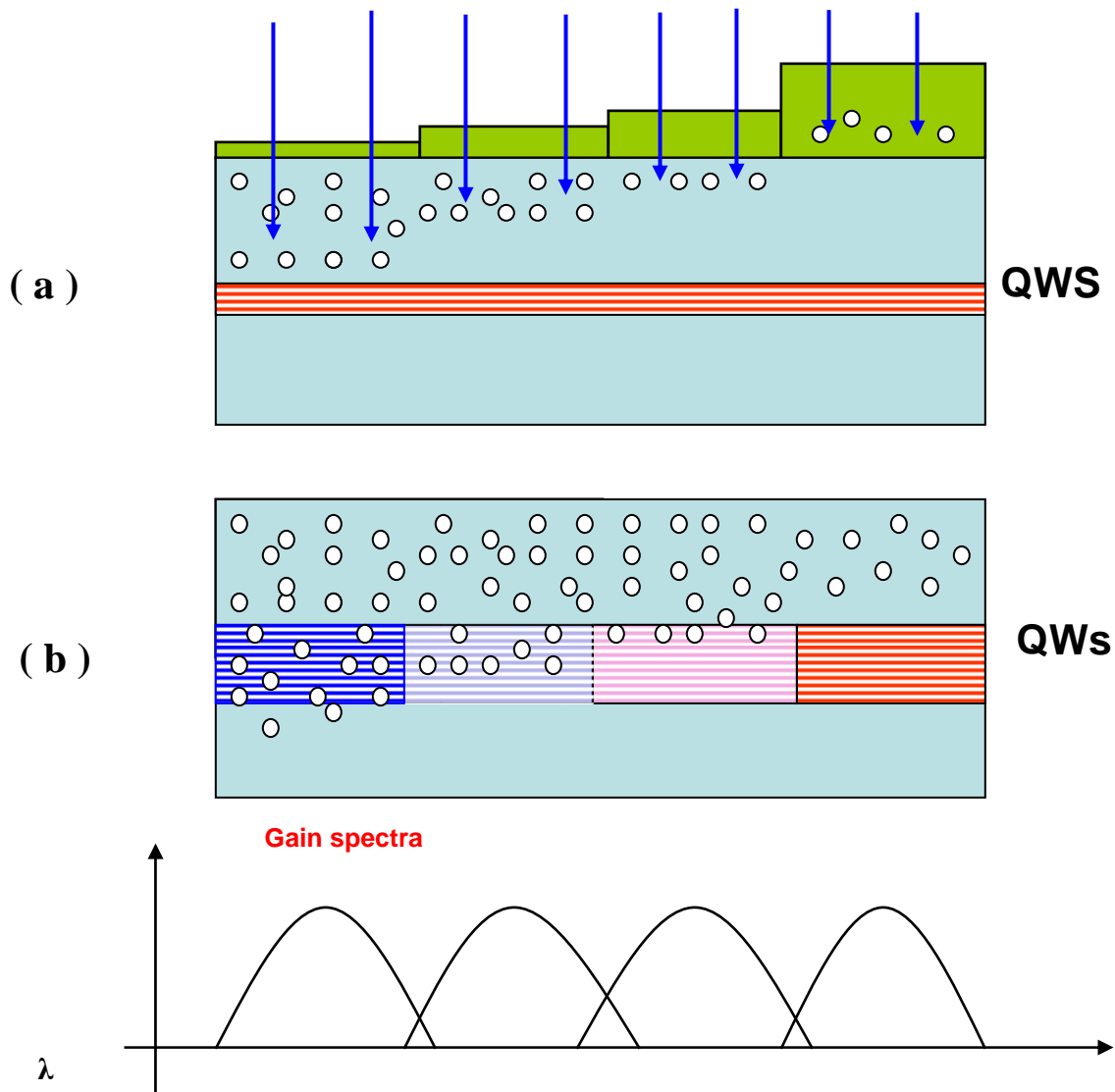


Figure 12
Schematic diagram of the wafer with different SiO₂ film thicknesses for ion implantation, and corresponding gain spectra for each area.

Some of the critical issues that must be considered for the QWI technology:

- The control of the bandgap profiles must make it possible to obtain the multi – peak – wavelength gain in different regions of a wafer, which meet pre-determined wavelengths for different lasers integrated in a laser array.
- There should be no or insignificant degradation of the intermixed material optical and electrical quality through the fabrication processes. This is an especially important issue with QWI process since they are based on an impurity generation mechanism.
- The lifetime of the intermixed devices should not be altered by the fabrication process.

We used the IEI method to do QWI. This technique has none of the obvious drawbacks shown in IID, IFVD, and PAID. In this technique, a two-step process was used to achieve the blue shift of the QW bandgap energies with different levels in the same chip. Step 1: SiO₂ mask with graded-thickness was fabricated on the sample, and stand ion implantation was performed through the SiO₂ mask as shown in Figure.12 (a). Step 2: After the SiO₂ mask was removed, an annealing of the samples was carried out using a rapid thermal annealer (RTA), and the wafers with multi – wavelength gain were fabricated as shown in Figure.12 (b).

After QWI, the gain peak of each region in the samples was shifted to the pre-determined wavelength. Then, laser arrays were fabricated, and the wavelength of each laser with DBR structure was designed at the gain - peak wavelength as shown in Figure.13.

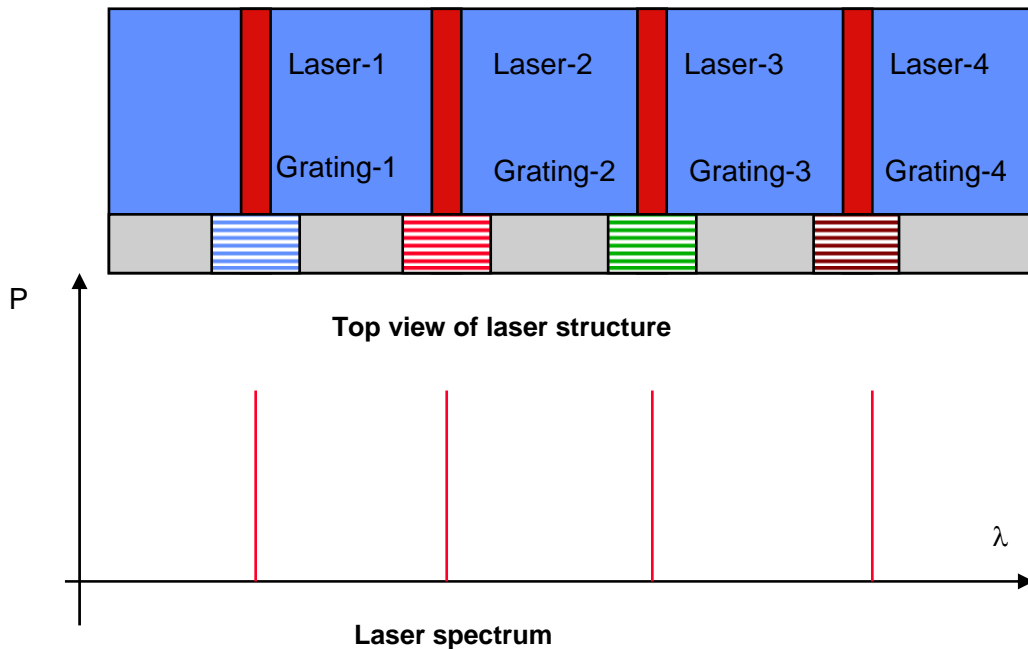


Figure 13
Schematic diagram of integrated laser array and corresponding laser spectra.

3 Laser array fabrications

The process steps of the laser array fabrications include wafer growth, quantum well intermixing of the wafers, grating fabrications, and DBR laser fabrications. The details are described in the paragraphs below.

3.1 Wafer growth

The wafers were grown by Metal-Organic Chemical Vapor Deposition (MOCVD) on n-doped InP substrate. After deposition of a 500 nm n^+ -InP buffer layer (Si doped $4 \times 10^{18} \text{ cm}^{-3}$) and 1200 nm n – InP lowering cladding layer (Si doped $1 \times 10^{18} \text{ cm}^{-3}$), the active region with 5 quantum wells centered at two separate-confinement layers 40 nm Q(1.05 μm) and 100 nm Q(1.156 μm) were grown. All of the quantum wells and the confinement layers were undoped. Then, an 200 nm “space” layer composed of 110 nm InP undoped and 90 nm InP (Zn doped $5 \times 10^{17} \text{ cm}^{-3}$), 50 nm stop layer (Zn doped $7 \times 10^{17} \text{ cm}^{-3}$), 1000 nm InP layer (Zn doped $7 \times 10^{17} \text{ cm}^{-3}$), and 100 nm InGaAs layer (Zn doped $2 \times 10^{19} \text{ cm}^{-3}$) were grown. Figure 14 shows the schematic diagram of laser layer structure.

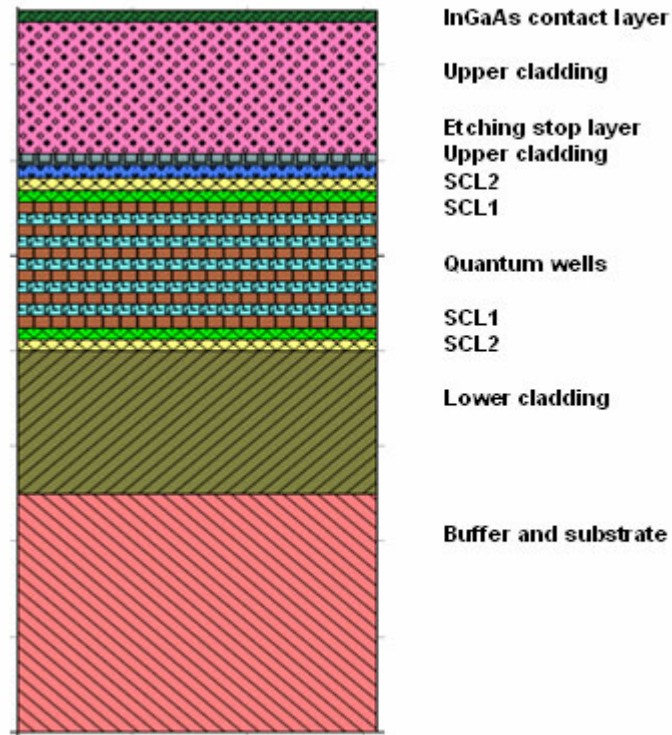


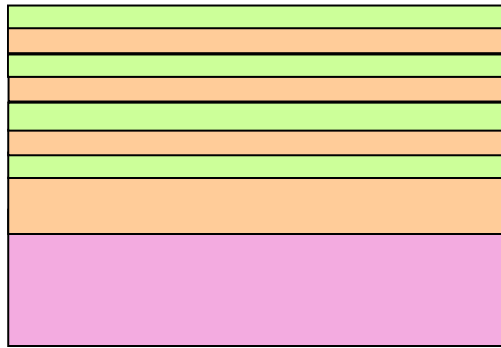
Figure 14
Schematic diagram of wafer layer structure.

3.2 Quantum well intermixing

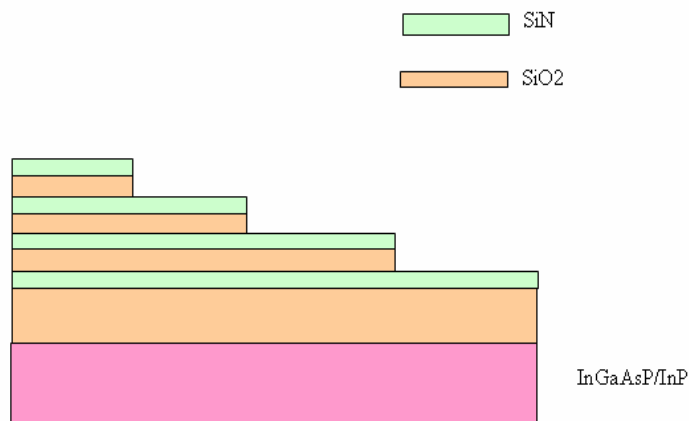
The flow chart of the QWI process is shown in Figure 15. After deposition of SiO₂/SiN multi-layer films, a select etching was used to make masks with different thicknesses by using BOE solution.

The etching rate of SiO₂ film in BOE solution is more than 20 times larger than that of SiN film. If the wet etching is used to do process, SiN film will be a good etching stop layer. Next, the implantation layer step was carried out. The implanted ion was phosphorus with 370 KeV energy and dose of 1.0×10^{13} ions/cm³. The wafer temperature was elevated to 200 °C throughout the implantation in order to avoid the formation of defect aggregates which have higher diffusion activation energy. The wafers were tilted at a 7° angle during implantation to reduce channeling effects. Following ion implantation, rapid thermal annealing was carried out at 700 °C for 120 S.

a. Deposit SiO₂/SiN multi-layer films



b. Select etching to make masks with different thicknesses



c. Ion implantation

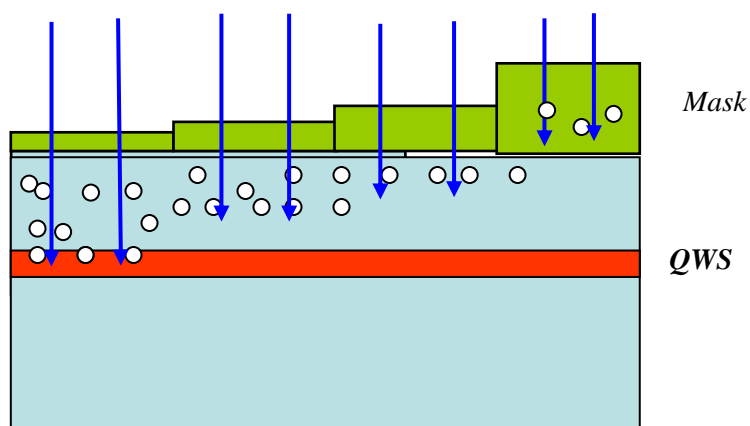


Figure 15

Flow chart of quantum well intermixing

Photoluminescence (PL) spectrum was then measured for each laser diode in the wafers to check the shift of the bandgap energies after QW intermixing. Since each laser diode is very small

(500 μm x 700 μm), it is important to create separation to avoid pumping the adjacent laser diodes during the test. No commercial equipment exists which could be used to isolate the pump for one laser diode of such diminutive size. Therefore, we built our own set-up to accomplish the PL test with the necessary isolation.

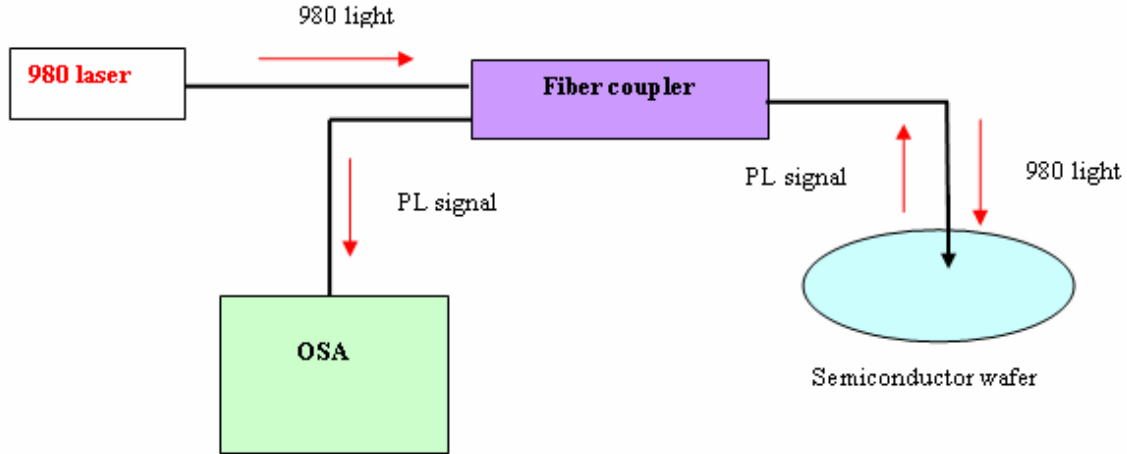


Figure 16
Schematic diagram of the set-up for PL tests of the wafers

Figure 16 shows the schematic diagram of the set-up APIC created for this special PL test. The 980 nm laser was used as the pump light source; the laser beam was focused into a fiber coupler to pump the semiconductor wafer. The photoluminescence signal (Wavelength region from 1400 nm to 1650 nm) from the QW inter-mixed wafer passed through the coupler to the optical spectrum analyzer (OSA). The section of the fiber tip was mounted on a holder, and the holder was fixed on a three axis stage with high precision, which was used to adjust the fiber tip position to focus the laser beam in the tested area. A microscope was used to check the positions of the fiber tip and the tested area.

The precision of the set-up for the focused laser beam position on the wafers could reach to 100 μm x 100 μm , which is sufficient to test the wafers.

This set-up was used to test the PL spectra for QW intermixed wafers. Figure 17 shows the tested PL spectra for the InGaAsP/InP wafer after QW intermixing. There are 4 PL spectra in the figure, which were taken from different areas with different thicknesses of SiO₂/SiN masks in the same wafer. The figure clearly shows the PL peaks shift with the thicknesses of SiO₂/SiN masks. Please note that the intensity of each gain curve is not normalized with each other.

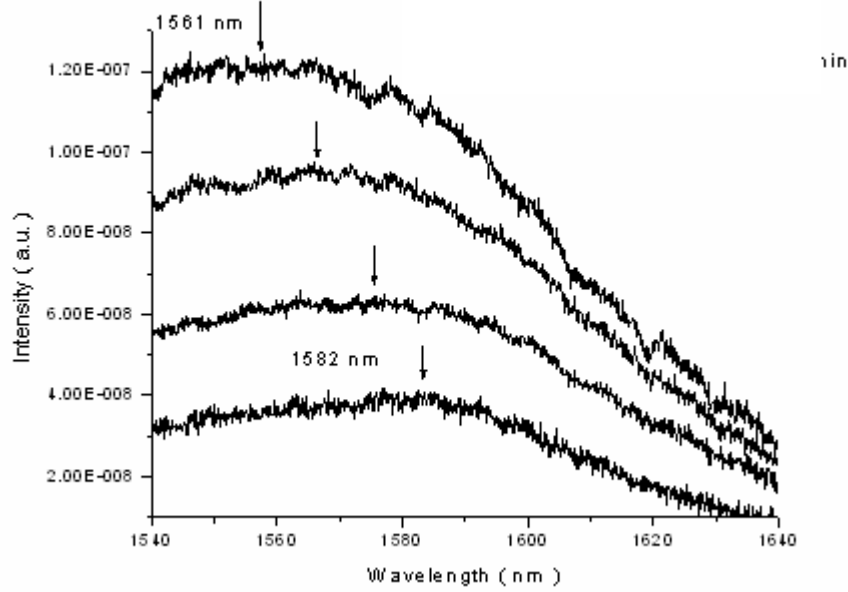


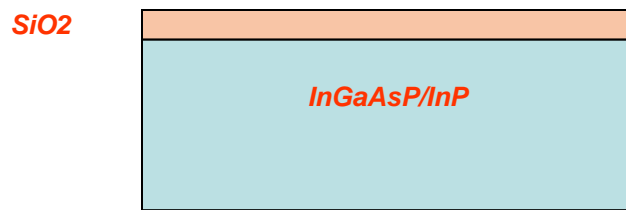
Figure 17
PL spectra of the wafer after QW intermixing. Each spectrum was taken from the area with different thicknesses of the SiO₂/SiN films.

3.3 Grating fabrications

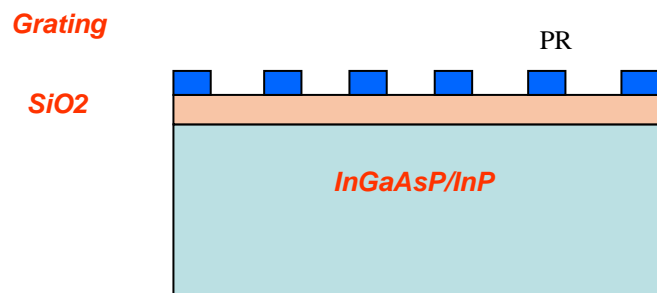
The traditional optical mask aligner could not be used to generate such grating patterns with pitches of ~ 242 nm, and the holographic exposure could not generate grating patterns with different pitches. We used an E-Beam writer to print the grating patterns.

Figure 18 is the flow chart of grating fabrications. Firstly, SiO₂ film was deposited on the InGaAsP/InP wafer. Then, the grating mask was printed on the SiO₂ film using an E-beam writer. Next, the SiO₂ film was etched by ICP to transfer the grating patterns into the SiO₂ film layer. Finally, the transferred SiO₂ mask was used to etch the grating in the InGaAsP/InP wafer. The gratings were the first-order surface gratings. The etching depth of the grating was ~ 1.1 μm .

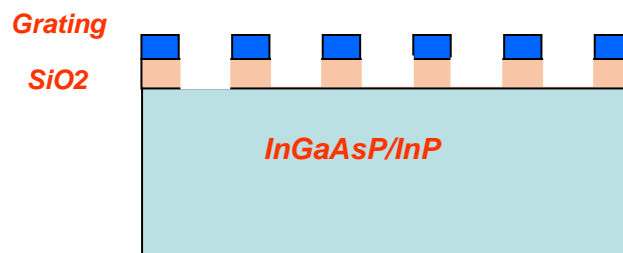
a. Deposit SiO₂ on InGaAsP/InP



b. Print grating mask by EB writer



c. Transfer(Etch) EB-generated grating into SiO₂ film



d. Etch grating by using SiO₂ mask



Figure 18
Follow chart of grating fabrications

Figure 19 shows a scanning-electron-microscope (SEM) picture of our grating patterns. Three different grating pitches were written: 242 nm, 244.5 nm, and 247 nm for three lasers in an array.

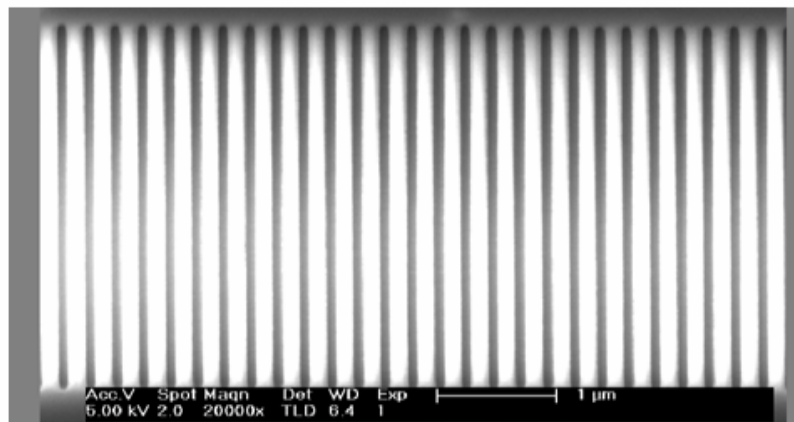
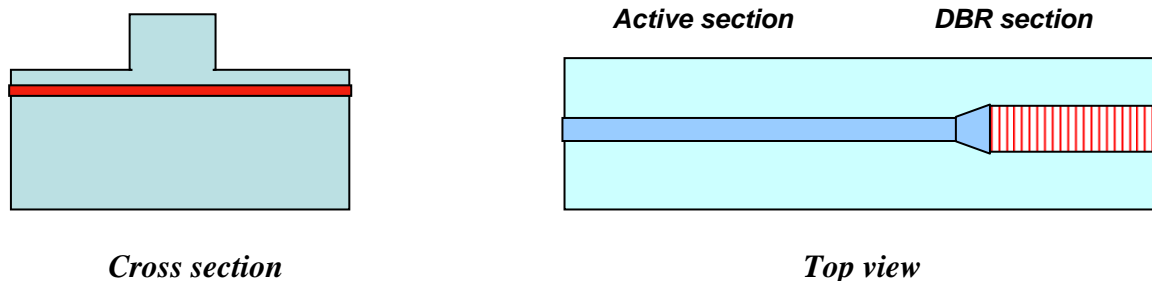


Figure 19
SEM picture of E-Beam generated grating pattern.

3.4 DBR Laser Fabrications

After the QWI and the grating processes, the final step was to fabricate DBR laser arrays. Figure 20 (*a* through *e* below) shows the flow chart of the DBR laser array fabrications. First, a ridge was etched in the gain and grating sections of the laser. The ridge is 1.1 μm deep. The ridge had different widths in gain and DBR sections. They were 4 and 6 μm, respectively. To ensure a good match of the power transition from gain section to DBR section, a power - match section between gain and DBR section was formed. Any mismatch between gain and DBR sections could lead to a coupling loss. A selective wet etching was used to form the ridge, the first etching solution was $\text{H}_2\text{SO}_4:\text{H}_2\text{O}_2$ (30%): H_2O (1:8:80) to remove the InGaAs cap layer, and then etching in $\text{HCl}:\text{CH}_3\text{COOH}$ (1:1) to selectively remove the InP layer positioned above the etch stop layer.

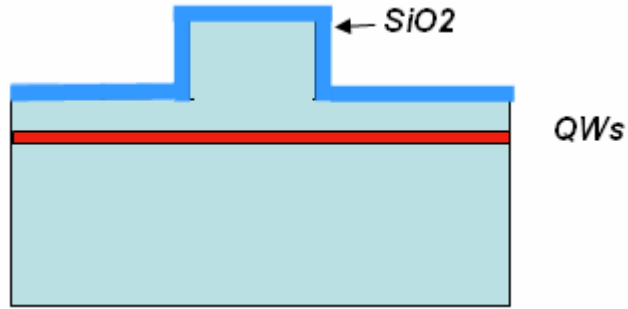
a. Make ridge in the active and DBR sections after grating fabrication.



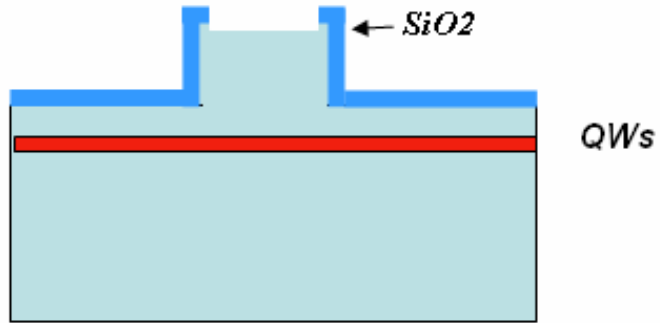
After the ridge was formed, SiO_2 film was deposited on the samples. Then a contact window was opened on the top of the ridge. The width of the window was 3 μm in the gain section and 5 μm in the DBR section. P-metal consisting of Ti/Pt/Au films were deposited by electron-beam-

evaporation for P-type contact. A lift-off metallization was aligned over the edge of the active section to electrically isolate the gain section pad and the DBR section pad as shown in Figure. 21. Finally, the samples were thinned to $\sim 120\text{ }\mu\text{m}$, an n-electrode consisting of Au/Ge/Ni and Au was deposited on the n-InP substrate. The laser arrays were cleaved to form an active-region length of $500\text{ }\mu\text{m}$ and DBR region length of $250\text{ }\mu\text{m}$.

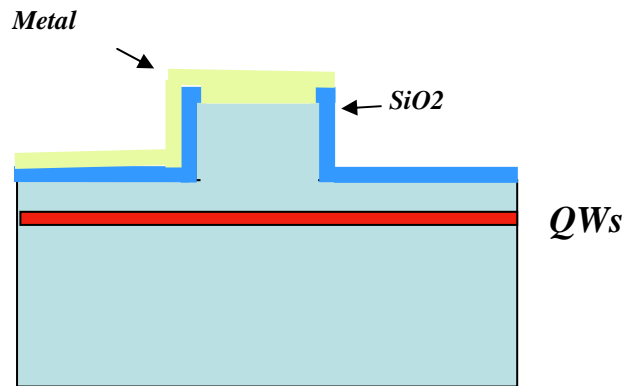
b. Deposit SiO₂ film



c. Open window on the top of ridge



d. Deposit metal for P-contact



e. Thin down InP substrate and deposit metal for N-contact

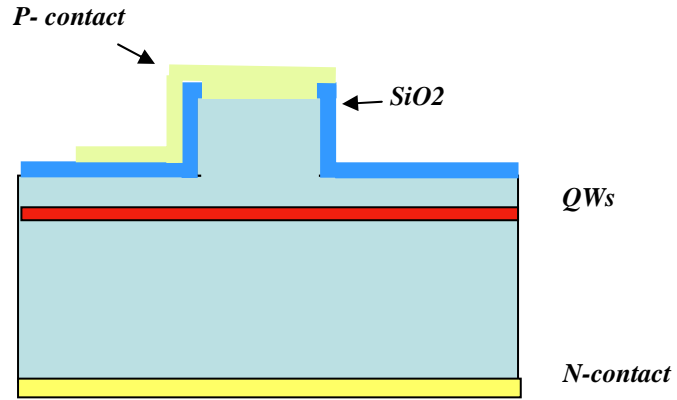


Figure 20
Flow chart of DBR laser fabrications.

Figure 21 shows a picture of laser array (top view). There are two electrode pads on the top of the array for wire bonding of the DBR and gain sections, respectively. The two-metal-pad separation is 15 μm for electrical isolation between DBR and gain sections.

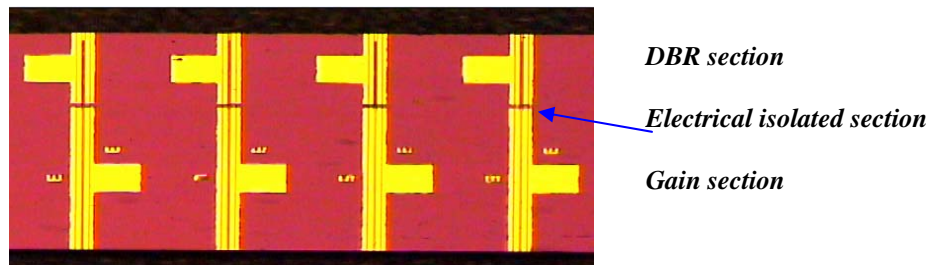


Figure 21
Picture of laser array (top view).

4 Test methods of laser array characteristics

4.1 Laser spectrum tests

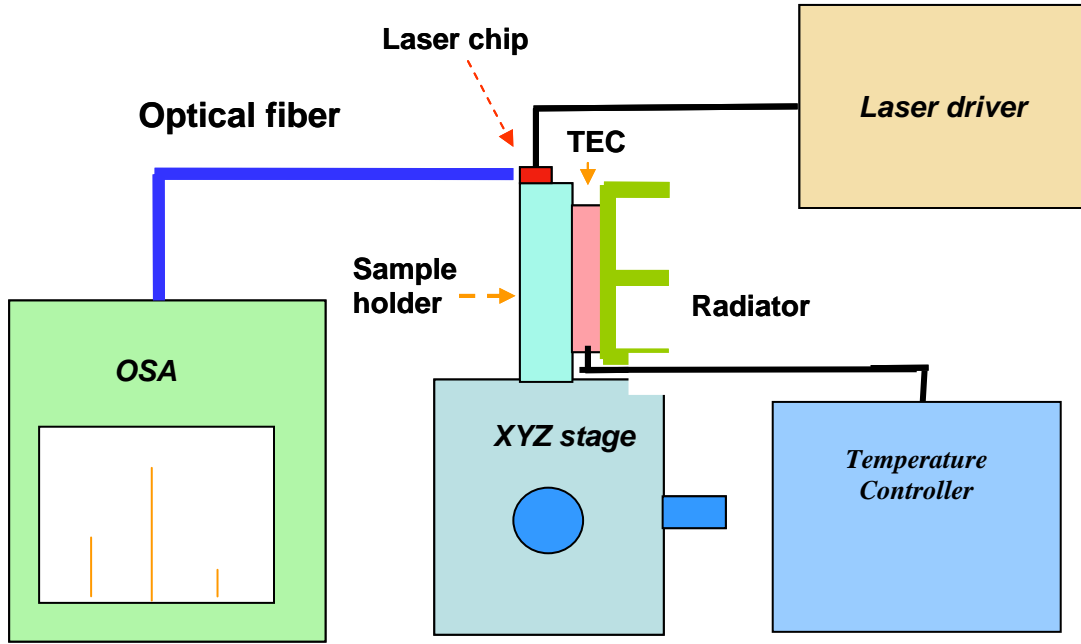


Figure 22
Schematic diagram of set-up for laser spectrum tests.

Figure 22 is the schematic diagram of the set-up for laser spectrum tests. The laser driver was used to apply DC bias to lasers, and Thermal-Electrical Cooler (TEC) was used to keep the tested lasers at a constant temperature, which was controlled by a temperature controller. The laser beam was focused into a fiber, and the optical spectrum analyzer (OSA) with the resolution of 0.01 nm was used to take laser spectrum data. From tested laser spectrum, the laser wavelengths and side-mode suppression ratio of each channel, and channel spacing of the laser arrays were determined.

4.2 Laser P-I and I-V tests

To determine the laser threshold current, output power, and quantum efficiency, we have to test laser output power as a function of the injected current (P-I characteristics). The laser forward voltage as a function of the injected current (I-V characteristics) is also important to determine a laser characteristics of P-N junction and Ohmic contact. Figure 23 shows the schematic diagram of the set-up for laser P-I and I-V characteristic tests. It is similar to that of the set-up shown in Figure. 22. Only difference is that an optical power meter with a larger area detector was used to take data instead of OSA. The area of the photodetector is 1 cm × 1 cm, which is large enough to cover the laser beam.

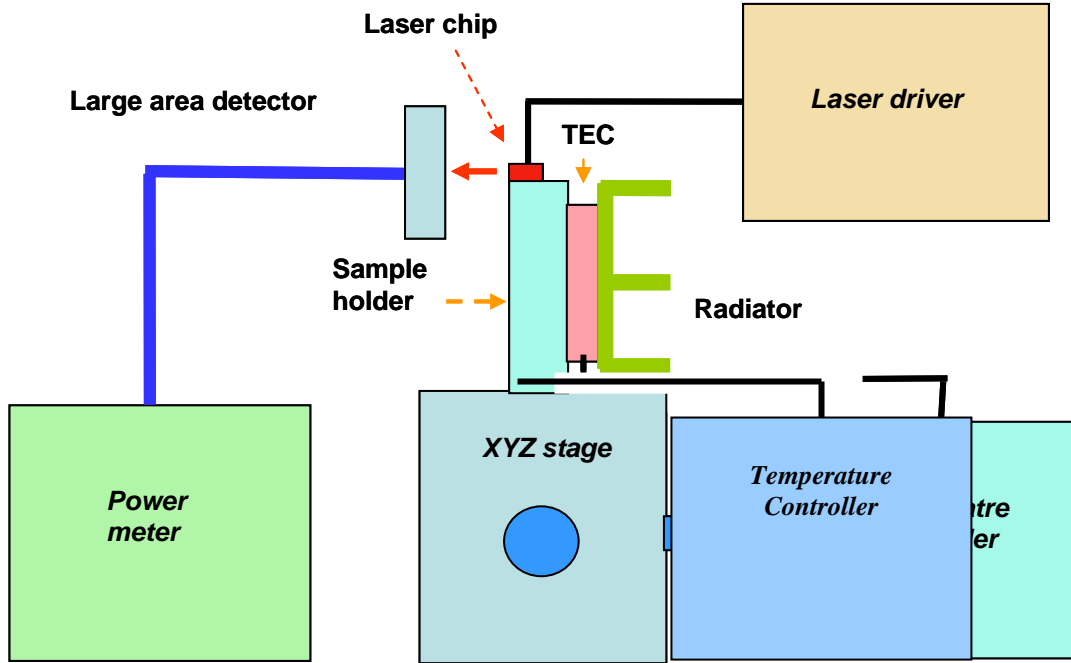


Figure 23
Schematic diagram of set-up for laser P-I and I-V tests.

4.3 Laser data rate and frequency response tests

Figure 24 is the schematic diagram of the set-up for laser data rate tests. A bias T was used to connect DC and AC signal to the laser, and a high-frequency probe was used to contact the tested laser. The laser was DC biased above the threshold current. The digital data signal from the BER

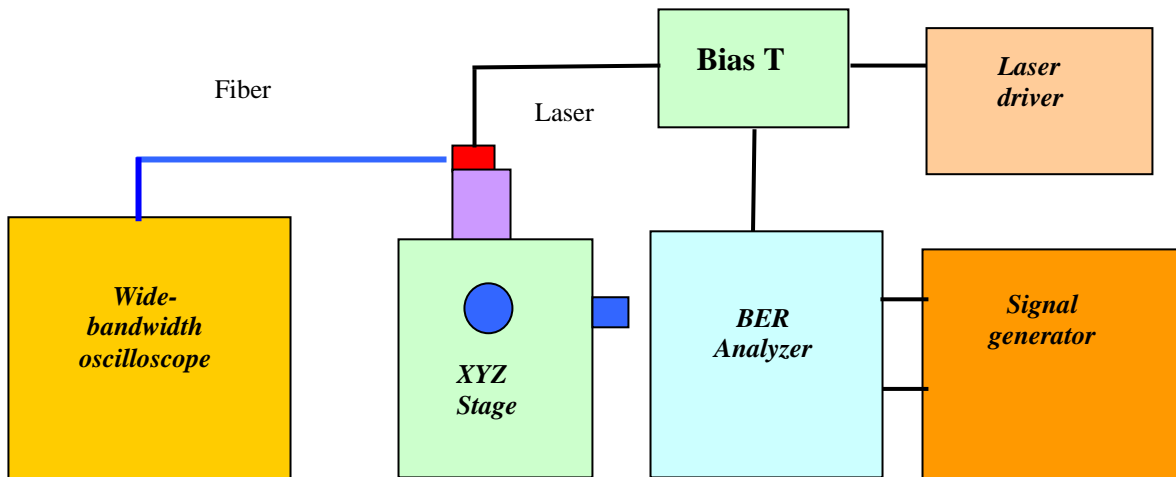


Figure 24
Schematic diagram of set-up for laser data rate tests.

(Bit Error Rate) test equipment was applied to the laser. The laser beam was focused into a fiber, and the wide-bandwidth oscilloscope was used to measure the output signal from lasers. The

laser output signal was applied to the vertical input of the oscilloscope, while the data rate was used to trigger the horizontal sweep of the oscilloscope. This is a typical set-up for the test of eye pattern.

To conform the tested data rate of the lasers, we have also measured the laser modulation bandwidth at -3 dB. Figure 25 shows the schematic diagram of the set-up for laser frequency response tests. The tested laser was biased above threshold current, and was modulated by sinusoidal current from a signal generator. From tested laser output intensity as a function of modulated frequency, the laser modulation bandwidth at – 3dB was determined.

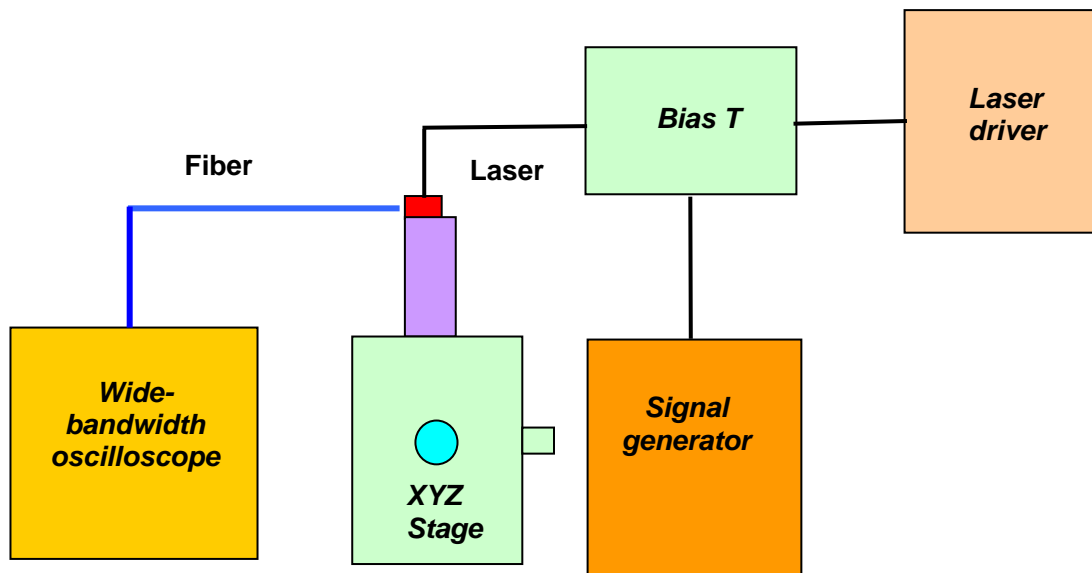


Figure 25
Schematic diagram of set-up for laser frequency response tests.

4.4 Laser linewidth tests

A homodyne technique was used to test laser linewidth. Figure 26 shows the schematic diagram of the test set-up. The laser was biased above threshold current. The laser emission was amplified by an optical amplifier, and was modulated by a Mach-Zehnder modulator with frequency of 5 GHz. Then, the lights were coupled into two arms of a single-mode fiber interferometer. The long interferometer arm was a long fiber, which provided a time delay. After the optical signals from the two interferometer arms were combined using a single-mode fiber coupler, they were mixed by an avalanche photodiode (APD). The beat signal centered at 5 GHz was displayed on a spectrum analyzer. The FWHM linewidth of a Lorentzian laser emission line was taken as one half the spectral width of the beat signal observed on the spectrum analyzer.

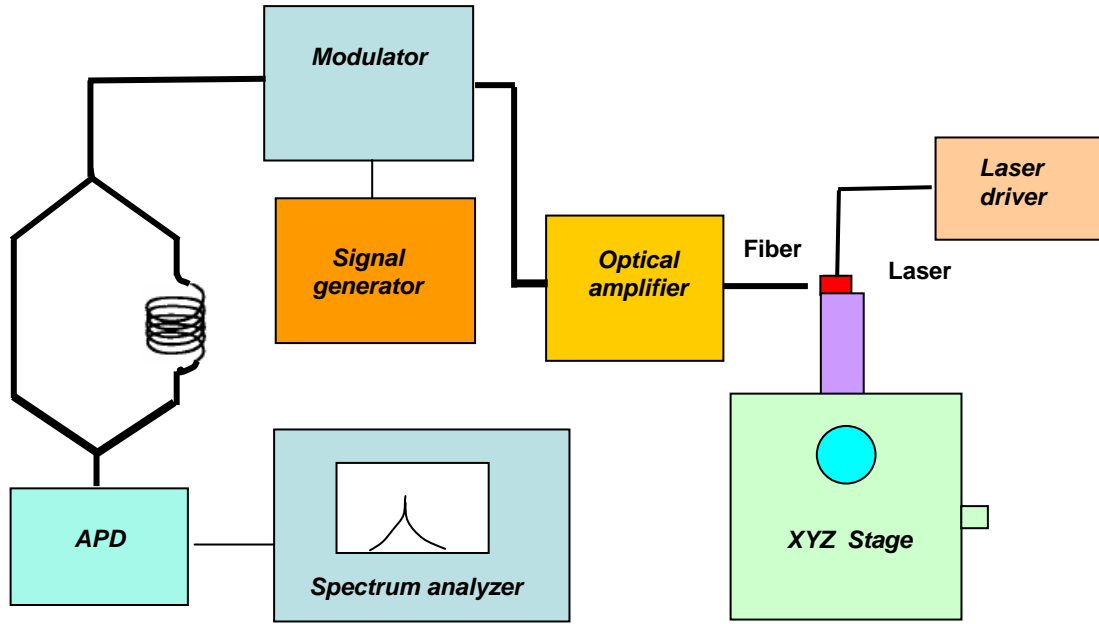


Figure 26
Schematic diagram of set-up for laser linewidth tests.

5 Tested results

Using the above test methods, we have measured the laser array spectrum, P-I and V-I characteristics, data rate and frequency response, and laser linewidth for many laser arrays. The typical results tested from a laser array are shown as follows. All data were taken at room temperature, and the DBR section of the lasers was biased at 10 mA.

5.1 Wavelength, channel space, and side - mode suppression ratio

Figure 27 is a tested laser array spectrum. Three wavelengths 1547.9 nm, 1563.0 nm, and 1578.2 nm were tested from three lasers in a laser array. It clearly shows that the channel spacing is ~ 15 nm, and laser side-mode suppression ratio is better than 35 dB.

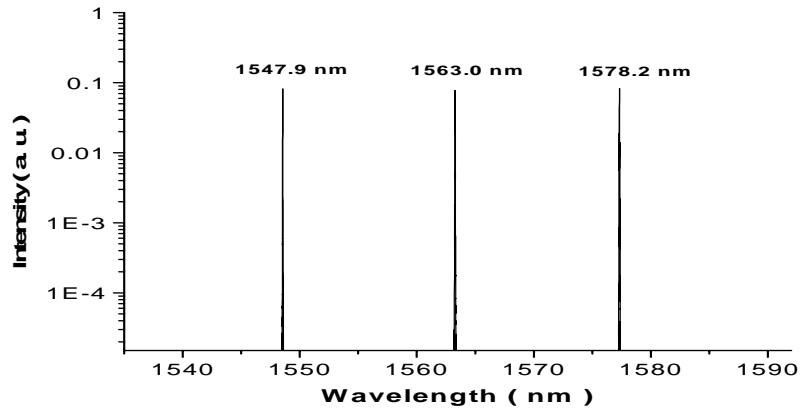


Figure 27
Laser array spectrum.

5.2 Threshold currents and output powers

The tested laser array P-I characteristics are plotted in Figures.28. Figure 28 (a) is the laser P-I characteristics tested from 3 different lasers in a laser array, which shows the threshold current of each laser is less than 30 mA. To test the maximum output power, we have increased the injected current to 100 mA for one laser as shown in Figure.28 (b). We observed the laser maximum output power of ~8 mW. It should be mentioned that the laser facets were not coated. After coating, the laser maximum power will be increased, and the threshold current will be decreased.

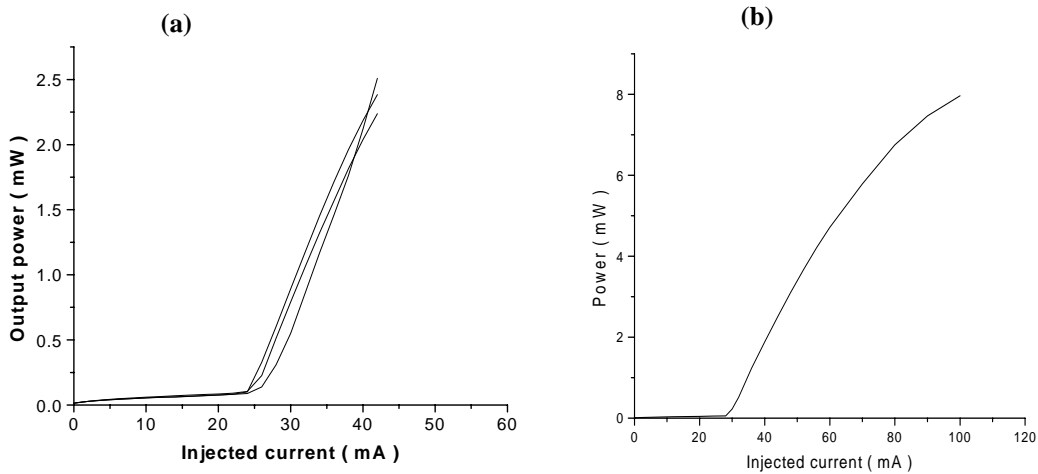


Figure 28
Laser P-I characteristics
(a) tested P-I from 3 different lasers in the laser array
(b) maximum output power tested from a laser in the laser array

Figure 29 is a typical laser I-V characteristic tested from a laser in the laser array, which shows that the laser turn on voltage is 0.7 V, and the laser forward resistance is $\sim 7.4 \Omega$, which was calculated from the slope of the I-V curve.

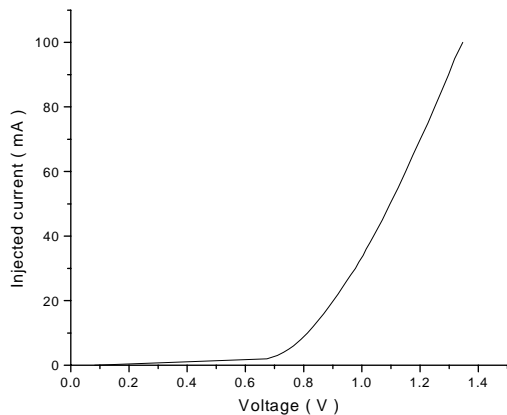


Figure 29
Laser I-V characteristics tested from a laser in the laser array.

5.3 Data rate and -3 dB bandwidth

We have tested the laser frequency response by using the set-up shown in Figure.25. The tested laser was biased at 40 mA, and the results are plotted in Figure.30. It shows that the bandwidth at -3dB is 5 GHz.

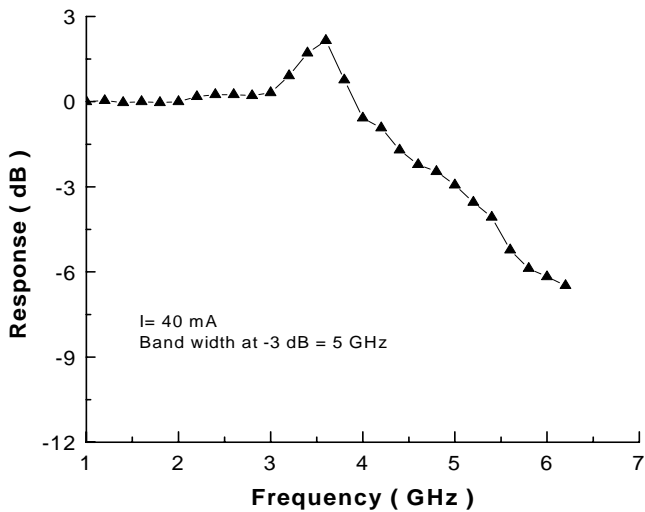


Figure 30
Laser frequency response.

To study the laser data rate, we have also tested the laser eye pattern. Figure 31 is an eye pattern tested from a laser at modulated frequency of 5 GHz.

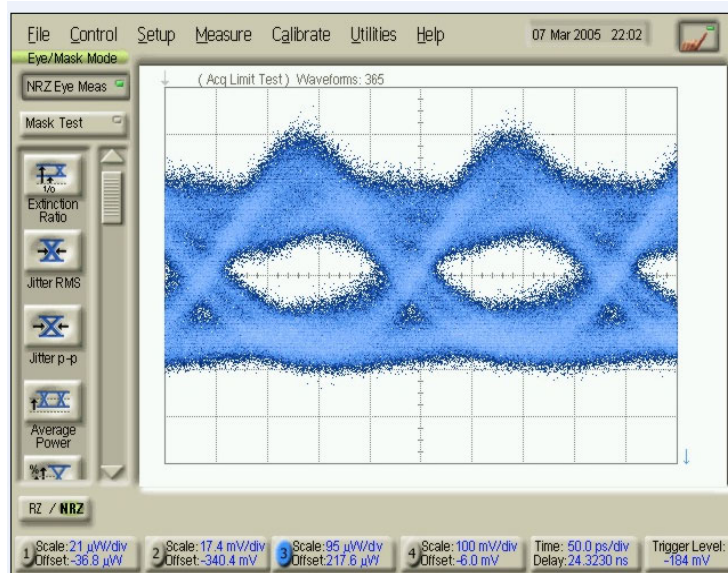


Figure 31
5 Gb/s eye pattern tested from a laser in the array.

5.4 Laser linewidth

Figure 32 shows the line shape of the homodyne signal measured from a laser in the array by using the set-up described in Figure.26. The beat signal centered at 5 GHz, and the FWHM linewidth of 15 MHz for the laser emission line could be obtained from the figure.

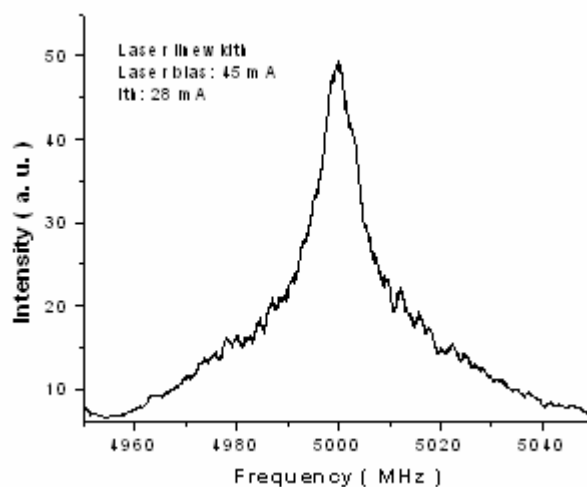


Figure 32
Line shape of the heterodyne signal tested from a laser in the array.

6 Summary

The above results clearly show that we have successfully designed and fabricated the laser arrays. The tested laser array performance meets the designed specifications, and some of the laser characteristics are better than the designed specifications.

To compare the above tested characteristics with the designed specifications of the laser arrays, we put all of the tested data into Table 3, and the designed specifications of the laser arrays are also listed in the Table. It clearly shows that the laser side-mode suppression ratio, maximum output power, data rate, and linewidth are better than the designed specifications.

Items	Designed Specification	Tested data
Channel number	3	3
Channel spacing (nm)	15	15
Side-mode suppression ratio (dB)	≥ 30	≥ 35
Threshold current per channel (mA)	≤ 30	≤ 30
Maximum output power per channel (mW)	≥ 1	≥ 5
Linewidth per channel (MHz)	< 1000	15
Data rate per channel (Gb/s)	2.5	5
Distance between two lasers (μm)	250	250

Table 3 - List of tested laser array performance and designed specifications.

In summary, we have successfully solved some issues of laser array design and processes in Phase I, the details have been described in the previous monthly reports. We have gained a lot of experience in the fabrication of the laser arrays, which is very valuable to make laser array with more complex structure in the next phase.

References

- [1]. L. V. Asryan, N. A. Gun'ko, et al. *Semiconductor Science Technology*, Vol.14, P.1069, 1999.
- [2]. H. Wada, K. Takemasa, T. Munakata, M. Kobayashi, and T. Kamijoh, *IEEE J. Select. Topics Quantum Electron.*, Vol. 54, p.420, 1999.
- [3]. P. J. A. Peter, L. F. Tiemeijer, J. J. M. Binsma, and T. V. Dongen, *J. Quantum Electronics*, Vol. 30, p.477, 1994.
- [4]. H. Kogelnik and C. V. Shan, *J. Appl. Phys.*, Vol. 43, p.2327, 1972.
- [5]. N. Holonyak, Jr., *IEEE J. Select. Topics Quantum Electron.*, Vol. 4, p.584, 1998.
- [6]. D. Deppe and N. Holoyak, *J. Appl. Phys.*, Vol. 64, p.93, 1988.
- [7]. S. K. Si, H. Yeo, K. H. Yoon, and S. J. Kim, *IEEE J. Select. Topics Quantum Electron.*, Vol. 4, p.619, 1998.
- [8]. A. McKee, C. McLean, G. Lullo, et al., *IEEE J. Quantum Electron.*, Vol. 33, p.45, 1997.
- [9]. B. Qui, A. Bryce, R. De La Rue, and J. Marsh, *IEEE Photon. Techol. Lett.*, Vol. 10, p.769, 1998.
- [10]. S. Charboneau, E. S. Koteles, et al., *IEEE J. Select. Topics Quantum Electron.*, Vol. 4, p.772, 1998.
- [11]. M. Paquette, V. Aimez, J. Beauvais, et al., *IEEE J. Select. Topics Quantum Electron.*, Vol. 4, p.741, 1998.
- [12]. H. S. Lim, V. Aimez, B. S. Ooi, *IEEE Photon. Techol. Lett.*, Vol. 14, p.594, 2002.
- [13]. H. Kogelnik, "Theory of optical waveguide," T.Tamir, Ed. New York, Spring-Verlag, 1988 ch. 2, p.43.